Estimation of Hydrodynamic Forces on Cylinders Undergoing Flow-induced Vibrations based on Modal Analysis

Guang Yin[a1], Marek Jan Janocha[a], Muk Chen Ong[a]

[a]Department of Mechanical and Structural Engineering and Materials Science, University of Stavanger

Stavanger 4036, Norway

Abstract

The objective of the present study is estimating hydrodynamic forces acting on cylinders undergoing vortex-induced-vibration (VIV) using Dynamic Mode Decomposition (DMD). The cylinders are subjected to a uniform incoming flow at a laminar Reynolds number ($Re = 250$) and an upper transition Reynolds number ($Re = 3.6 \times 10^6$) ($Re = U_\infty D/\nu$ defined based on the incoming flow U_∞, the diameter of the cylinder D and the viscosity of the fluid ν). Both a single cylinder and a configuration of piggyback cylinders are considered. Numerical simulations based on two-dimensional URANS (Unsteady Reynolds Averaged Navier-Stokes) equations combined with the $k-\omega$ SST turbulence model are carried out to obtain the snapshots of the surrounding flow fields for DMD analysis. The DMD method is a powerful tool to obtain the spatial-temporal evolution characteristics of the coherent structures in the wake flow behind the cylinders. In the present study, this modal decomposition method is combined with a moving reference frame around the cylinders. The dominant DMD modes with their corresponding frequencies of the wake flows are identified and are used to reconstruct the flow fields. The large-scale shedding vortices are captured by the dominant modes. The reconstructed wake flow behind the cylinders is used to estimate the drag and lift forces on the cylinders combined with a force partitioning analysis.

Keywords: Modal decomposition; Vortex-induced-vibration; Hydrodynamic forces.

1. Introduction

Vortex induced vibration (VIV) is a commonly observed fluid-structure-interaction phenomenon. In offshore technology, VIV will lead to a reduction of fatigue life of many structures such as risers, power cables and pipelines. VIV denotes oscillatory motions of structures caused by the force resulted from the Karman vortex shedding in the wake of the structures. When the vortex-shedding frequency is synchronized with the structural nature vibration frequency, there is an oscillation with a large amplitude, which is termed as lock-in. To design effective methods of reducing the vibration amplitude of VIV, it is important to understand the wake flow behind the structure and its relationship with the hydrodynamic forces acting on the structure. In addition, the Reynolds number of the incoming flow, the mass ratio and the damping ratio of the structure can also influence VIV. There are extensive experimental and numerical studies on VIV of cylindrical structures. The physics of VIV can be investigated using an idealized model of an elastically mounted circular cylinder free to vibrate with two degree-of-freedom (2Dof). The wake flows behind a cylinder undergoing VIV display complicated coherent flow structures which lead to unsteady hydrodynamic forces on the cylinders. Most of the current studies usually investigated the hydrodynamic forces and performed spectrum decomposition of their time histories to obtain their characteristic frequencies such as Zhao et al. [1], Janocha & Ong [2] and Serta et al. [3]. Qualitive analysis of the wake coherent flow structures was performed by using vortical structures identification. However, the underlying relationship between the wake vortical structures and the frequency components of the hydrodynamic forces acting on the cylinders has not been uncovered. Recently, modal decomposition analysis has been developed to extract dominant coherent flow structures and understand their spatial and temporal behaviors. The most employed modal

decomposition methods are the proper orthogonal decomposition (POD) introduced by Lumley [4] and the dynamic mode decomposition (DMD) introduced by Schmid [5] as well as their variants. After these dominant coherent flow structures are extracted, a reduced-order model of the flow system can be built.

Most of the applications of modal decomposition analysis considered the flows around stationary structures while there are a few studies on fluid-structure-interaction systems. The main challenge in applying modal decomposition on fluid-structure-interaction systems is the difficulty in dealing with the moving boundaries of the structures. Liberge & Hamdouni [6] computed POD modes based on a global velocity field in the domains including both the fluid and solid and built a low-dimensional dynamical system of the FSI system. Freno et al. [7] proposed a modified POD method using dynamic basis function to analyze flow data on deforming meshes. Yao & Jaiman [8] developed ROM of flows around a transversely vibrating cylinder using an eigensystem realization algorithm. Miyanawala & Jaiman [9] used POD to analyze dominant flow features of FSI systems. Wang & Shoele [10] proposed a POD algorithm combined with a conformal mapping technique on FSI systems with deforming geometries. Shinde et al. ([11], [12]) constructed a Galerkin-free ROM of flows around a vibrating cylinder using POD modes. Shinde & Gaitonde [13] developed Lagrangian variants of POD and DMD to treat the moving bodies in flows. In contrast to the POD modes which are optimal in their energy content while containing multiple frequencies, the extracted DMD modes are characterized by their dynamics and each DMD mode has its own single frequency. For VIV, there is complicated frequency spectra distribution due to the interaction between the wake flow and the body motions, which brings challenge to the understanding of the underlying flow physics and the relationship between the coherent flow structures and hydrodynamic forces. According to various previous studies such as Rowley et al. [14], Noack et al. [15], Towne et al. [16] and Ping et al. [17], the DMD method can provide a best-fit linear approximation of complicated nonlinear flow systems and identify the flow structures with spatial coherency as well as their characteristic frequencies and growth/decay rates. Furthermore, by carrying out numerical simulations or experiments, the obtained flow fields such as the velocities and the vorticities are of multiple frequencies. The commonly employed postprocessing method such as Fourier decomposition can only provide frequency spectra for time-histories of drag and lift coefficients or a signal at a single point. However, DMD can extract spatial structures with their frequencies. As a result, the obtained DMD frequency spectra also contain spatial coherency. In analogy to the idea presented in Guzmán-Iñigo et al. [18], the modes extracting using DMD can be regarded as dataset training. After the dominant modes are learned, the overall flow systems can be reconstructed and approximately represented. Furthermore, by using their characteristic frequencies, the future evolutions of the wake flows can be predicted. A similar method has also been used in Yu et al. [19]. Therefore, the DMD method is suitable to extract dominant modes with different temporal dynamics information. Especially, the obtained DMD modes are more related to the frequency components of the dynamical systems compared with other modal decomposition analysis.

Furthermore, most of the previous modal decomposition analysis focused on extracting the coherent flow pattern around structures and developing dynamical systems to investigate their evolutions. In VIV, the structural motions are determined by the hydrodynamic forces caused by the wake vortices. Therefore, it is important to uncover the relationship between these extracted dominant modes and the forces on the immersed structures, which has not been sufficiently discussed. In the present study, a DMD analysis of the wake flow behind a vibrating cylinder and a piggyback configuration of two cylinders is performed. The focus is on the estimation of the drag and lift forces on the cylinders using the extracted DMD mode. A force partitioning method is used to relate the forces on the cylinders with the surrounding flows without directly integrating the pressure and the viscous stress on the surfaces of the cylinders.

The paper is organized as follows. Section 2 presents the computational overview of the numerical simulations to obtain the data of the wake flow behind the vibrating single cylinder and the piggyback

configuration as well as the modified modal decomposition method used to extract the DMD modes of the FSI systems. Section 3 gives the results and discussion of the modal decomposition analysis results and the estimated forces on the cylinders using a finite number of DMD modes. Cases at a high Re up to $Re = 3.6 \times 10^6$ are considered. The conclusion is given in Section 4.

2. The computational overview

2.1 Governing equations, the computational domain, the boundary conditions and the numerical methods

The two-dimensional (2D) numerical simulations to obtain the flow fields snapshots for the DMD analysis are carried out using the finite-volume code OpenFOAM based on the incompressible unsteady Reynolds-Averaged Navier–Stokes (URANS) equations for the high Re turbulent flow:

$$\frac{\partial \overline{u}_i}{\partial t} + \frac{\partial \overline{u}_i \overline{u}_j}{\partial x_j} = -\frac{\partial \overline{p}}{\partial x_i} + \frac{\partial \overline{\tau}_{ij}}{\partial x_j} - \frac{\partial \overline{u'_i u'_j}}{\partial x_j}$$ (1)

$$\frac{\partial \overline{u}_i}{\partial x_i} = 0$$ (2)

where $\overline{u}_i$ and $\overline{u}_j$ are the mean velocity components, u'_i and u'_j are the fluctuating velocity components ($i, j = 1,2$ denote the streamwise and the cross-stream directions which are also denoted as x, y with their corresponding velocity components u, v), $\overline{p}$ is the mean pressure, $\overline{\tau}_{ij}$ is the mean viscous stress tensor. The Reynolds stress tensor $\overline{u'_i u'_j}$ is resolved using the $k - \omega$ SST turbulence model. A detailed description of this method can be found in Menter [20] which is not presented here. For the low Re laminar flow the unsteady Navier-Stokes equations are solved directly, hence the Reynolds stress tensor is not included in the simulations. The PIMPLE algorithm which is a hybrid of the Semi-Implicit Method for Pressure-Linked Equations (SIMPLE) and the Pressure-Implicit with Splitting of Operators (PISO) algorithms is employed to solve Eqs (1) and (2). The second order Crank–Nicolson method is used for the time integration. The convective term is discretized using Gauss linear scheme with a flux limiter and a second-order central difference scheme is used for other spatial derivatives. An adjustable time-step is based on the Courant number (Co) criterion to ensure that the value is less than 1 at each time step for all the simulated cases. For each simulation, at least 10 vortex shedding cycles are simulated to sample the flow data.

A single cylinder with diameter of D and a piggyback with two rigidly coupled cylinders in which the main cylinder with a diameter of D and a smaller cylinder with diameter of $d = 0.2D$ placed on top of the main cylinder with a gap of $G/D = 0.125$ between their surfaces are considered in the present study. The piggyback cylinders configurations are widely used in engineering. Their hydrodynamic characteristics have been extensively investigated in Yang et al. [21], Janocha & Ong [2] and Serta et al. [3]. The computational domain and the boundary conditions for the numerical simulations are set the same as those used in Serta et al. [3] and Janocha et al. [22]. Detailed mesh and time-step convergence studies to determine the optimal grid and time-step resolutions as well as the validation studies for the present numerical model have already been conducted in Janocha et al. [22] and Serta et al. [3] and are not presented in the present study. A body fitted hexahedral grid is used near the cylinders for the simulation and a H-grid topology is used in the far field. An example of the mesh for the single cylinder and the piggyback is shown in Fig 1. The parameters for all investigated cases are shown in Table 1. The reduced velocity is defined as $U_r = f_n D/U_\infty$ where f_n is the natural frequency of the system in a vacuum

Table 1 Cases for the modal decomposition analysis in the present study.

Case	Configurations	Re	Reduced velocity U_r
1	Piggyback cylinders	250	5
2	Single cylinder	3.6×10^6	6
3	Single cylinder	3.6×10^6	7
4	Single cylinder	3.6×10^6	12
5	Piggyback cylinders	3.6×10^6	7
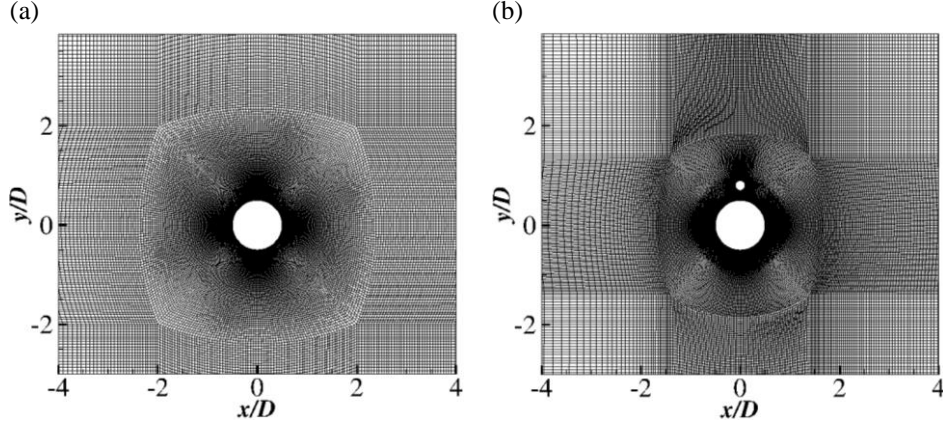
FIGURE 1: Example of the mesh details around the cylinders (a) the single cylinder; (b) the piggyback cylinders.

2.2 Dynamic Mode Decomposition with a moving structure

The Dynamic Mode Decomposition method introduced by Schmid [5] is used to extract coherent flow structures with their corresponding single frequencies. A reduced order representation of the spatial-temporal information of the flow data can be obtained by the DMD method as

$$\mathbf{u}(x, y, z, t) \approx \sum_{i=1}^{N} a_i \boldsymbol{\psi}_i \exp(i\lambda_i t) \tag{3}$$

where $\boldsymbol{\psi}_i$ is the spatial mode along with their corresponding amplitude a_i and λ_i is the complex frequency of each mode. The temporal information of each mode is embedded in λ_i where $\text{Im}(\lambda_i)$ is the temporal growth and $\text{Re}(\lambda_i)$ is the frequency. The modes that make the most contribution to the dynamical system can be extracted using sparsity-promoting algorithm (SPDMD) introduced by Jovanovic et al. [23] on the original DMD method. The mathematical details of DMD and SPDMD are not repeated in the present study as they have already been used in many other studies such as Schmid [5], Jovanovic et al. [23], Statnikov et al. [24], Wu et al. [25], Janocha et al. [22]. The streamwise and cross-flow velocities, the spanwise vorticity as well as the structural velocities at each time step are sampled for the DMD analysis. To reduce the memory of matrix decompositions in the DMD analysis of the flow data, an on-the-fly incremental Singular Value Decomposition (SVD) algorithm is used in the present study. The algorithm is also used by Ohmichi [26], Matsumoto & Indinger [27] and Yin & Ong [28].

The current applications of the DMD method are mainly on analysis the surrounding flow fields around a stationary body in a fixed reference frame. However, the modal analysis for flows around moving bodies is rare. Modal decomposition analysis has been performed on a body-fitted moving mesh under the Arbitrary Lagrangian-Eulerian (ALE) framework in Janocha et al. [22]. However, it was shown in Menon & Mittal [29] that if the original DMD method is directly used for a moving body, the shape of the body is not correctly

captured in the reconstructed flow fields using the resulting DMD modes because the regions inside the body switch between being occupied by the body and occupied by the fluid flows. Therefore, a modification to the original DMD method by introducing a moving frame was introduced in Menon & Mittal [29] and was applied for the flow around a sinusoidally pitching airfoil. This modified DMD method using a moving reference frame along with the moving body is also used in the present study shown in Fig. 2, which is different from that employed in Janocha et al. [22]. The coordinates inside the moving reference frame are denoted as ξ and the flow field data in the moving frame is denoted as $\mathbf{u}(\xi)$. It should be mentioning that the body is fixed inside the moving reference. Then, the DMD modal analysis can be performed for the data in the moving reference frame and the flow quantities can be reconstructed with the modes $\psi_i(\xi)$ also defined on the coordinates in the moving frame as

$$\mathbf{u}(\xi, t) \approx \sum_{i=1}^{N} a_i \psi_i(\xi) \exp(i\lambda_i t) \qquad (4)$$

The modes $\psi_i(\xi)$ in the moving frame can be mapped to the fixed 'lab-frame' as $\psi_i(x)$ through interpolations. Finally, the reconstructed flow field in the fixed 'lab-frame' should also include the relative velocity field $\mathbf{r}(x)$ between the moving frame and the fixed 'lab-frame' as $\mathbf{u}(x, t) \approx \sum_{i=1}^{N} a_i \psi_i(x) \exp(i\lambda_i t) + \mathbf{r}(x)$. The relative velocity fields can be also decomposed as $\mathbf{r}(x) = \sum_{i=1}^{N} a_{ri} \psi_{ri}(x) \exp(i\lambda_i t)$ in analogy to (3). In the present study for cylinders under VIV, this relative velocity is the induced velocity of the cylinders, which should be the same at all points in the moving frame.
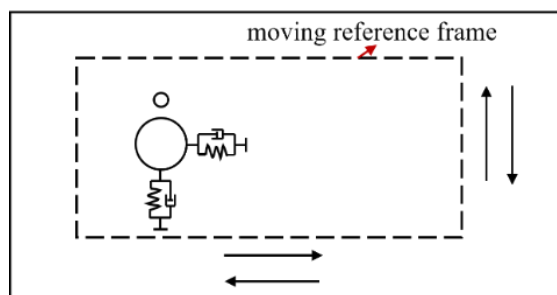
FIGURE 2: Sketch of the moving reference frame of the modal decomposition analysis.

According to Chang [30], the total aerodynamic or hydrodynamic force components F_i ($i = x, y$ in the streamwise and cross-stream directions) on an immersed structure can be decomposed as

$$F_i = -\oint \phi_i \frac{\partial \mathbf{u}}{\partial t} \cdot \mathbf{n} dS + \frac{1}{2} \oint |\mathbf{u}|^2 \mathbf{n} \cdot \mathbf{e}_i dS - \int (\mathbf{u} \times \boldsymbol{\omega}) \cdot \nabla \phi_i dV + \nu \oint (\boldsymbol{\omega} \times \mathbf{n}) \cdot (\nabla \phi_i + \mathbf{e}_i) dS \qquad (4)$$

by using auxiliary potentials ϕ_i which satisfy the following equation and boundary conditions:

$$\nabla^2 \phi_i = 0 \text{ inside the flow field} \qquad (5)$$
$$\nabla \phi_i \cdot \mathbf{n} = \mathbf{e}_i \cdot \mathbf{n} \text{ at the body surface} \qquad (6)$$
$$\nabla \phi_i \cdot \mathbf{n} = \mathbf{0} \text{ at the outer boundaries} \qquad (7)$$

This force partitioning can reveal different contributions to the total forces due to different mechanisms. The first two surface integration terms of the right-hand side in Eq. (4) are the contribution made by the body motions, which consists of body acceleration with $\partial \mathbf{u}/\partial t$ and body kinetic energy $|\mathbf{u}|^2$. For a rigid body, it can be shown that the contribution due to the body kinetic energy since the velocities on the body surface $\mathbf{u}_s$ remain unchanged with the coordinates and $\oint |\mathbf{u}|^2 \mathbf{n} \cdot \mathbf{e}_i dS = |\mathbf{u}_s|^2 \oint \mathbf{n} \cdot \mathbf{e}_i dS = |\mathbf{u}_s|^2 \int \nabla \cdot \mathbf{e}_i dV = 0$. The third volume integration terms in Eq (4) are due to the vorticity within the whole flow fields. Finally, the last surface integration terms in Eq. (4) are made by the surface vorticity

contributions. It should be mentioned that Eq. (4) are derived by multiplying the gradient of the auxiliary potential with the original NS equation. For RANS equations, despite of the terms in Eq. (4), there is a remaining term associated with the Reynolds stress. However, this term can be deemed negligible because contributions to the total forces due to the eddy viscosity are much smaller than the contributions made by the vorticity. By using this force partitioning method, the relationship of the forces on the body and the surrounding flow fields can be quantified, which has been adopted in Martín-Alcántara et al. [31], Moriche et al. [32], Zhang et al. [33] and Menon & Mittal [34]. Also, the main part of the forces can be estimated by using the wake flow data using this partitioning method, which has been adopted in Wang et al. [35] and Tong et al. [36]. For the present study, since the wake flow of the vibrating cylinders can be approximated by using dominant DMD modes, the contributions of the DMD modes on the forces acting on the cylinders can be quantified.

3. Results and discussion

As seen in the force partitioning formulas in Eq. (4), the components of velocity $\mathbf{u}$ and vorticity $\boldsymbol{\omega}$ in the flow domain and the vorticity on the cylinders' surfaces $\boldsymbol{\omega}_s$ and structural velocities are required to obtain the forces. Therefore, snapshots in the present study consist of both the $\mathbf{u}$ and $\boldsymbol{\omega}$ fields. These quantities are used for modal decomposition analysis instead of using exclusively velocities or vorticities as commonly conducted in the previous studies such as Zheng et al. [37] and Janocha et al. [22] for the flow past moving structures. The spatial ranges of the moving reference frame as shown in Fig. 1 are $-5D \leq x \leq 25D$ in the streamwise direction and $-8D \leq y \leq 8D$ in the cross-stream direction.

3.1 Low Re laminar flow case

According to Konstantinidis et al. [38], at the low $Re = 250$, although a three-dimensional instability might exist, the spanwise vorticity component is much higher than the other two components by one order. In addition, the influences of the three dimensionality of the wake flow on the force acting on the cylinder is weak. Therefore, the drag and lift forces on the cylinder are primarily determined by the two-dimensional wake flow instability and can be predicted using 2D simulations.

The DMD is performed using $N = 1000$ snapshots equidistantly distributed with a time step of $\Delta t U_\infty / D = 0.1$. Fig. 3 shows the DMD spectra with the DMD frequencies and their corresponding DMD amplitudes normalized by the mean mode amplitude. By using sparsity-promoting algorithm, there are four dominant DMD modes are identified and by using these four dominant modes, the approximation loss is only 20%, which indicate that up to 80% of total energy of the system can be captured by using these modes.
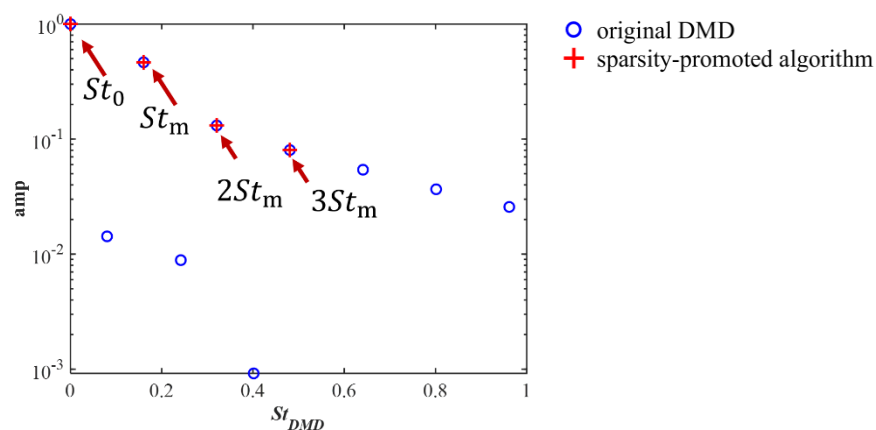
FIGURE 3: The frequency spectra of the DMD modes for Case 1 and the dominant modes denoted by the arrows (blue circles: the modes obtained by using the original DMD method and red crossings: the modes obtained by applying the sparsity-promoted algorithm).

Figs 4 and 5 shows time histories of the contributions of each term to the drag and lift forces reconstructed by using these dominant modes as Eq. (7). The forces reconstructed by using the dominant modes are compared with the forces obtained from the CFD simulations, which shows that each reconstructed force is almost the same with those obtained by the simulation. For the drag force, the volume integral of the drag coefficient $C_{D,\mathbf{u}\times\boldsymbol{\omega}}$ resulted from $\mathbf{u}\times\boldsymbol{\omega}$ are dominant in the forces compared with other contributions. The body motion induced drag coefficient C_{Dm} of the piggyback pipelines are fluctuating around 0 and its fluctuation amplitude is comparable to that of $C_{D,\mathbf{u}\times\boldsymbol{\omega}}$. For the lift force, the body motion induced lift force C_{Lm} is dominant compared with other terms. The time-histories of the body motion induced contribution is symmetric around their mean value of 0 with a single frequency while the time-history of $C_{L,\mathbf{u}\times\boldsymbol{\omega}}$ is asymmetric around 0 with two fluctuating modes.
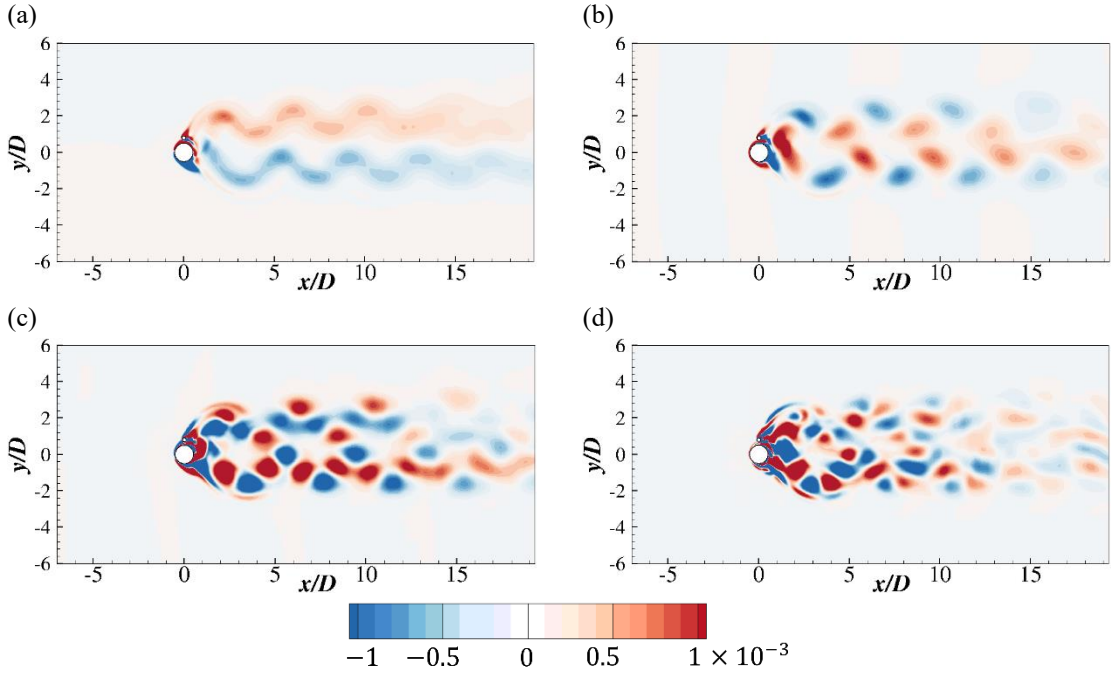
The spanwise vorticity ω_z contours of these dominant modes are shown in Fig. 6. Due to the low Re, the overall mode shapes tend to be regular. For these dominant modes, Mode 1 at a frequency of $St_{\mathrm{m}} = 0.16$ represents the cylinder motion induced mode. It can be observed that the cylinder motion is also coupled with some large-scale weak wake flow structures. The vortex shedding patterns are related with the high-order harmonics. For these high-order harmonics modes, the shear-layer structures are shown, and the increasingly smaller-scale structures compared with Mode 1 are generated. Close to the piggyback cylinder, the packet of these structures is oriented towards the top and bottom sides and in the further downstream locations, the small-scale structures tend to form parallel vortex rows to the streamwise direction.

(a) (b)
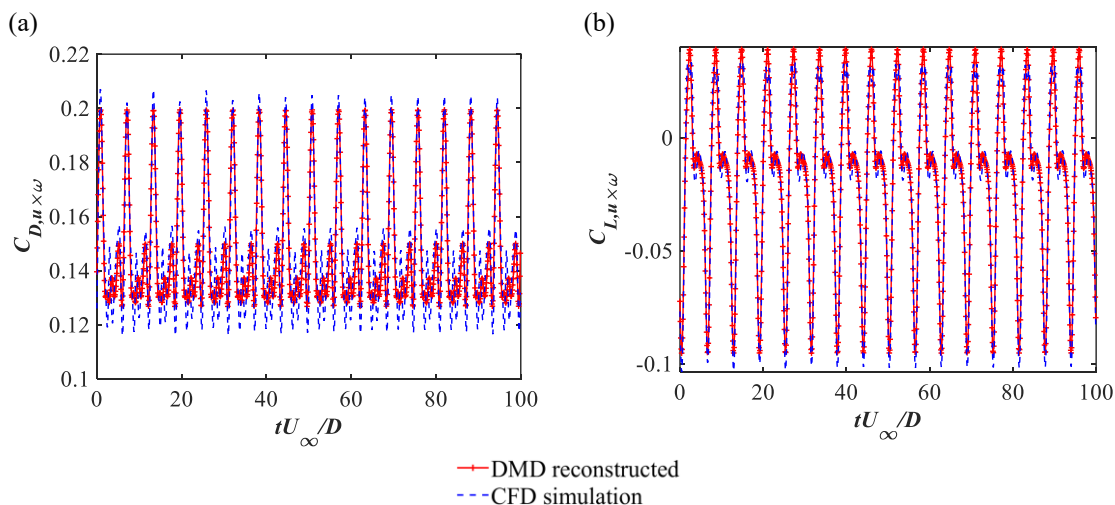
FIGURE 4: The time-histories of (a) the reconstructed volume integral of drag coefficient $C_{D,\mathbf{u}\times\boldsymbol{\omega}}$ (red crossings) compared with that obtained by the CFD simulation (blue dashed lines); (b) the reconstructed volume integral of the lift coefficient $C_{L,\mathbf{u}\times\boldsymbol{\omega}}$ (red crossings) compared with that obtained by the CFD simulation (blue dashed lines) for Case 1.
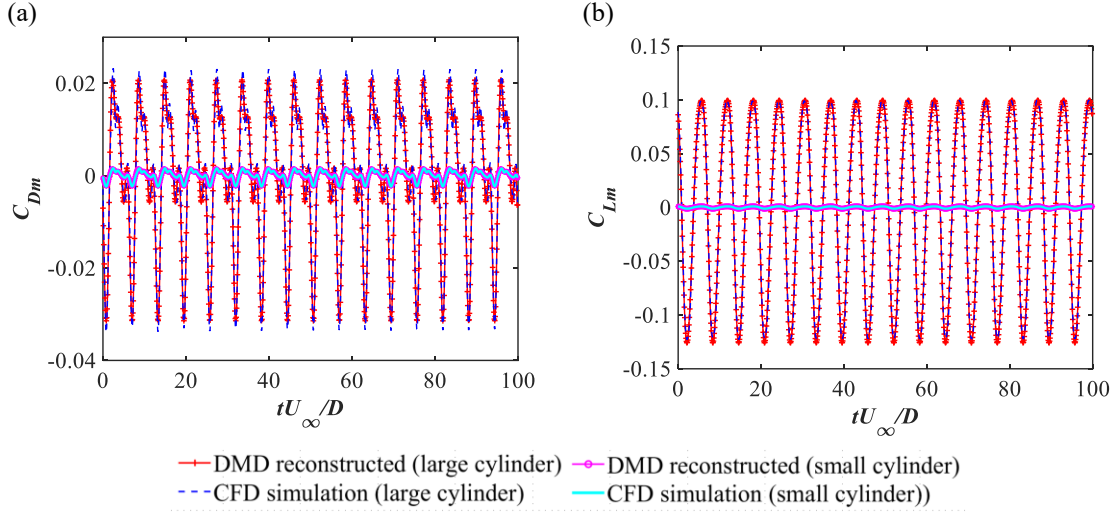
FIGURE 5: The time-histories of (a) the reconstructed body motion induced drag coefficient C_{Dm} (red crossings: the large cylinder; red circles: the small cylinder) compared with that obtained by the CFD simulation (blue dashed lines: the large cylinder; blue solid: the small cylinder); (b) the reconstructed volume integral of the lift coefficient C_{Lm} (red crossings: the large cylinder; magenta circles: the small cylinder) compared with that obtained by the CFD simulation (blue dashed lines: the large cylinder; cyan solid: the small cylinder) for Case 1.

FIGURE 6: The spanwise vorticity contours of the extracted dominant DMD modes shown in Fig. 3 for Case 1: (a) the mean flow mode at St_0; (b) the mode at St_m; (c) the mode at $2St_m$; (d) the mode at $3St_m$.

3.2 High Re turbulent flow case

For the high Re turbulent flow case with a single cylinder and $U_r = 6$, the DMD is performed using $N = 314$ snapshots equidistantly distributed with a time step of $\Delta t U_\infty / D = 0.08$. Fig. 7 shows the DMD

8

spectra. It can be seen that due to the chaotic feature of the flow behavior for this case, there are multiple modes identified and they are clustered around several peaks. After applying the sparsity-promoting algorithm, the four DMD modes corresponding to the mean flow, the cylinder vibration frequency, the second harmonic and the third harmonic mode are extracted, and the approximation loss is 33%. Due to the high Re, the contribution of the viscous effects to the hydrodynamic forces is small. Therefore, only the volume integral of $\mathbf{u} \times \boldsymbol{\omega}$ and the body motion induced terms are discussed here. For the drag and lift force, the time-histories of the reconstructed $C_{D,\mathbf{u}\times\boldsymbol{\omega}}$ resulted from $\mathbf{u} \times \boldsymbol{\omega}$ using the four retained dominant modes are shown in Fig. 8 compared with those obtained by carrying out CFD simulations based on Eqs (1) and (2). It can be seen that the overall oscillation patterns of the reconstructed forces are close to the simulations data. The differences between the reconstructed forces and the data from simulations are mainly observed at their peak values due to the truncation using a few modes. The time-histories of the reconstructed body motions induced lift coefficient C_{Lm} are almost the same as those of the simulations data. However, the reconstructed body motion induced drag coefficient C_{Dm} only displays sinusoidal temporal evolution. The chaotic behavior of the C_{Dm} time history cannot be reconstructed using four dominant modes as shown in Fig. 9 (a). In addition, due to the much larger cross-flow vibration amplitude than the streamwise vibration amplitude as shown in Serta et al. [3], the modes selection by using the DMD method is more biased towards the cross-flow motion. Therefore, the frequencies of the lift forces especially C_{Lm} are more accurately captured than the drag forces.

The spanwise vorticity of the mode shapes for the four dominant modes are shown in Fig. 10. These modes are symmetric about the x-axis. The mode corresponding to the cylinder vibration frequency in Fig. 10 (b) shows a strong motion induced surrounding flow closely around the cylinder. In the far wake region, this mode also shows weak and large-scale structures tilting towards upper and lower cross-stream directions, which may be related to a weak modulation of the vortex street. The mode at $2St_m$ shown in Fig. 10 (c) displays two rows of a clear vortex-shedding in the wake region, due to the 2P wake flow pattern. The 2P vortices pairs are represented by the alternative positive and negative vorticity of the mode. Fig. 10 (d) shows the third harmonic mode, which displays smaller-scale vortices and more chaotic flow features compared with the second harmonic mode.
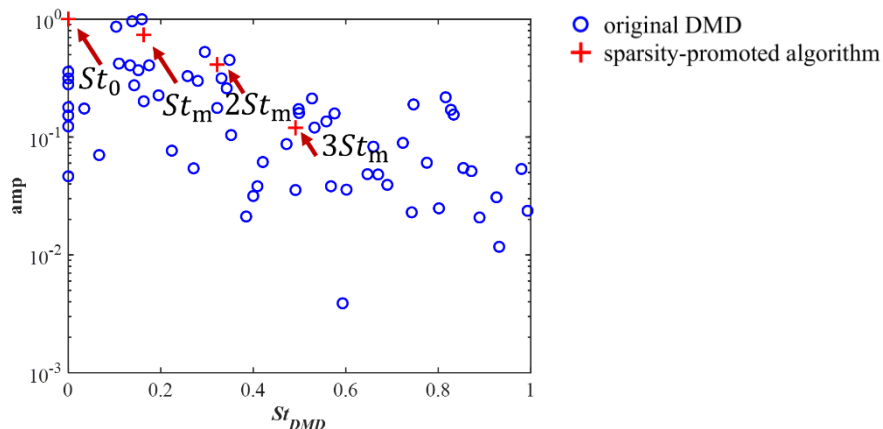

FIGURE 7: The frequency spectra of the DMD modes for Case 2 and the dominant modes denoted by the arrows (blue circles: the modes obtained by using the original DMD method and red crossings: the modes obtained by applying the sparsity-promoted algorithm).

9
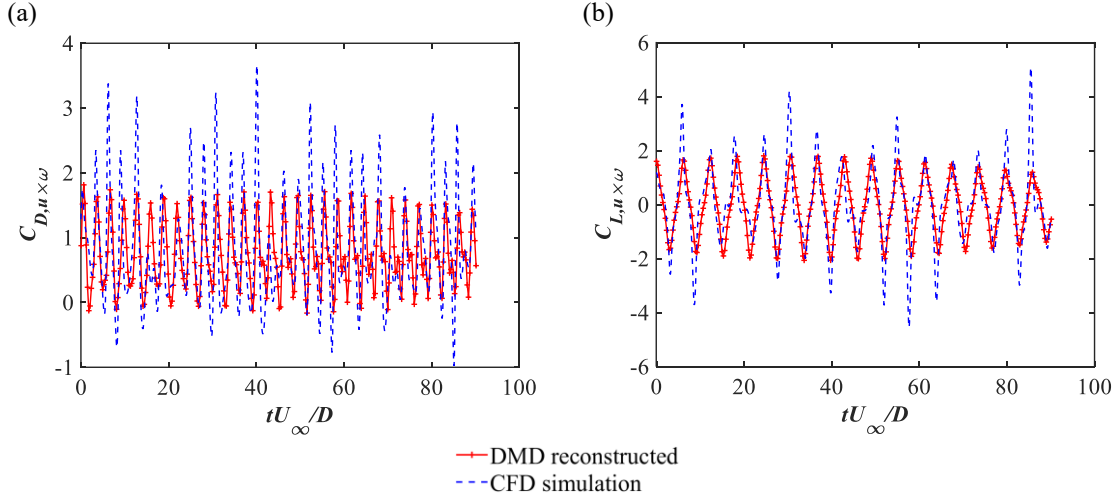
FIGURE 8: The time-histories of (a) the reconstructed volume integral of drag coefficient $C_{D,\mathbf{u}\times\boldsymbol{\omega}}$ (red crossings) compared with that obtained by carrying out the CFD simulation (blue dashed lines); (b) the reconstructed volume integral of the lift coefficient $C_{L,\mathbf{u}\times\boldsymbol{\omega}}$ (red crossings) compared with that obtained by carrying out the CFD simulation (blue dashed lines) for Case 2.
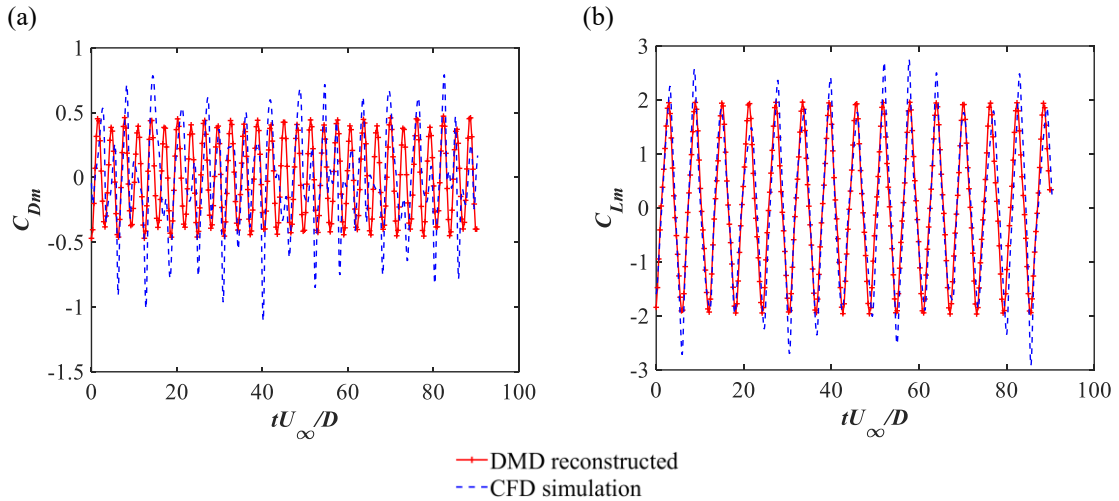
FIGURE 9: The time-histories of (a) the reconstructed body motion induced drag coefficient C_{Dm} (red crossings) compared with that obtained by carrying out the CFD simulation (blue dashed lines: the large cylinder); (b) the reconstructed volume integral of the lift coefficient C_{Lm} (red crossings) compared with that obtained by carrying out the CFD simulation (blue dashed lines) for Case 2.
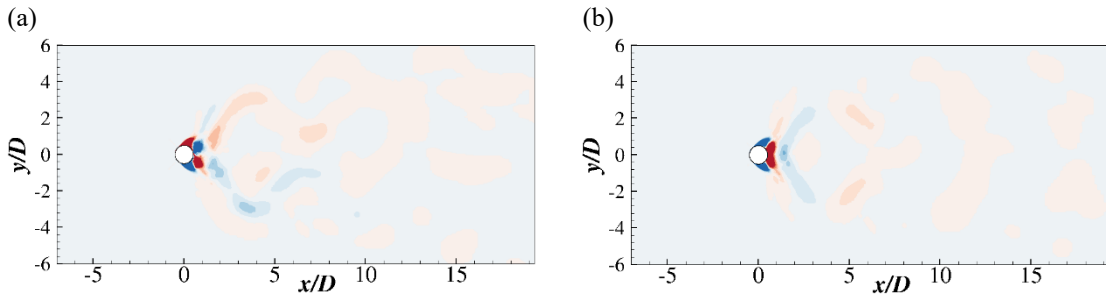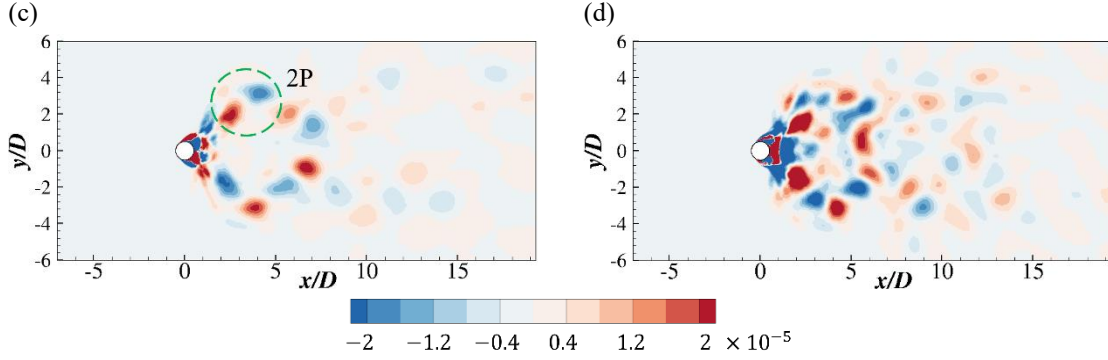
FIGURE 10: The spanwise vorticity contours of the extracted dominant DMD modes shown in Fig. 7 for Case 2: (a) the mean flow mode at St_0; (b) the mode at St_m; (c) the mode at $2St_m$; (d) the mode at $3St_m$.

For Case 3 with $U_r = 7$, a number of $N = 376$ snapshots equidistantly distributed with a time step of $\Delta t U_\infty / D = 0.08$ are used to perform the modal decomposition analysis. The DMD spectra for the $U_r = 7$ case are shown in Fig. 11. It can be seen that the flow behavior is regular and there are fewer modes identified compared with those for the $U_r = 6$ case. After applying the sparsity-promoting algorithm, the four DMD modes related to the mean flow, the cylinder vibration and their second and third harmonics are retained, which corresponds to approximately 80% of the total energy of the system. The time-histories of the reconstructed $C_{D,\mathbf{u}\times\boldsymbol{\omega}}$, $C_{L,\mathbf{u}\times\boldsymbol{\omega}}$, C_{Dm} and C_{Lm} using the four retained dominant modes compared with those obtained by carrying out the CFD simulations are shown in Figs. 12 and 13. Due to the regular wake flow and the motion pattern of the cylinder, the reconstructed results closely match the simulations data. The spanwise vorticity of the modes for the four dominant modes are shown in Fig. 14. Compared with those reported for Case 2 with $U_r = 6$, a clearer pattern can be observed from the mode shapes. The mode corresponding to the cylinder vibration frequency in Fig. 14 (b) shows two pairs of shear layers tilting towards the cross-stream directions. The obvious 2P vortex shedding pattern seems to be more clearly represented by the third harmonic mode compared with the second harmonic mode, which may represent a weak modulation of the vortex street.
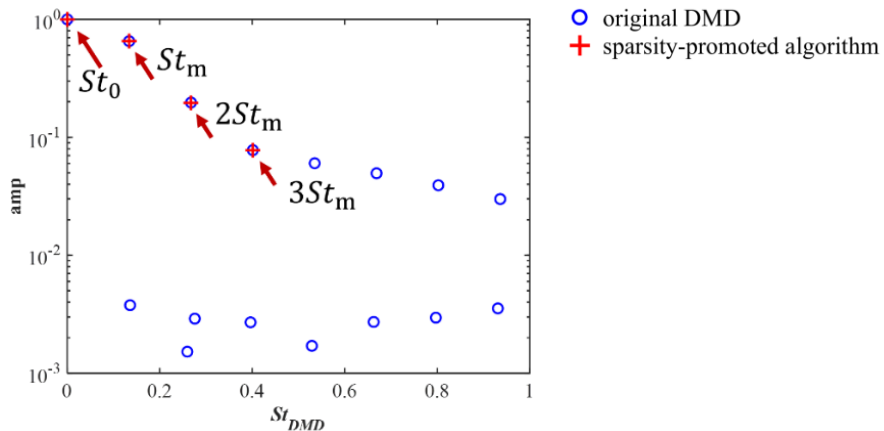

FIGURE 11: The frequency spectra of the DMD modes for Case 3 and the dominant modes denoted by the arrows (blue circles: the modes obtained by using the original DMD method and red crossings: the modes obtained by applying the sparsity-promoted algorithm).
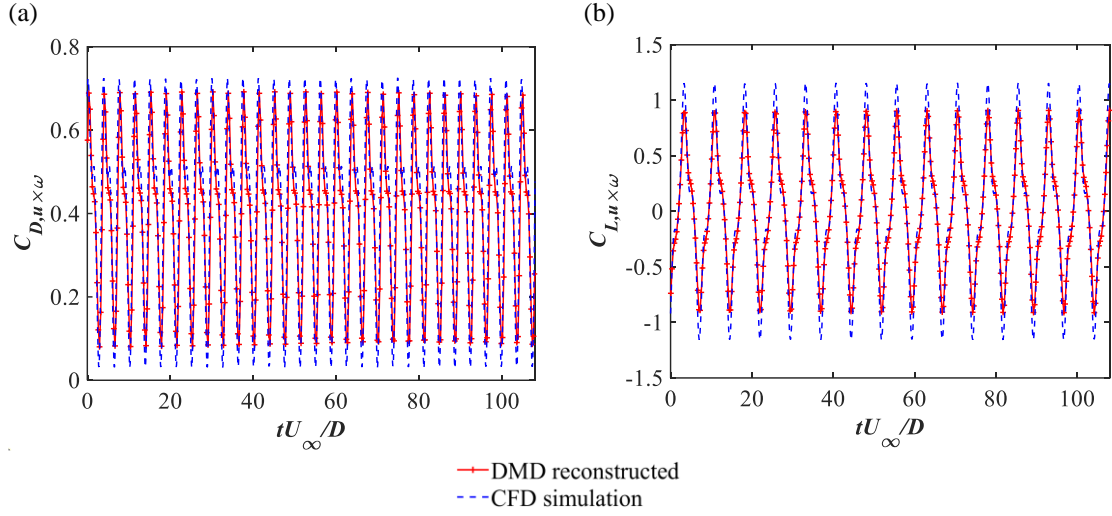
FIGURE 12: The time-histories of (a) the reconstructed volume integral of drag coefficient $C_{D,\mathbf{u}\times\boldsymbol{\omega}}$ (red crossings) compared with that obtained by carrying out the CFD simulation (blue dashed lines); (b) the reconstructed volume integral of the lift coefficient $C_{L,\mathbf{u}\times\boldsymbol{\omega}}$ (red crossings) compared with that obtained by carrying out the CFD simulation (blue dashed lines) for Case 3.
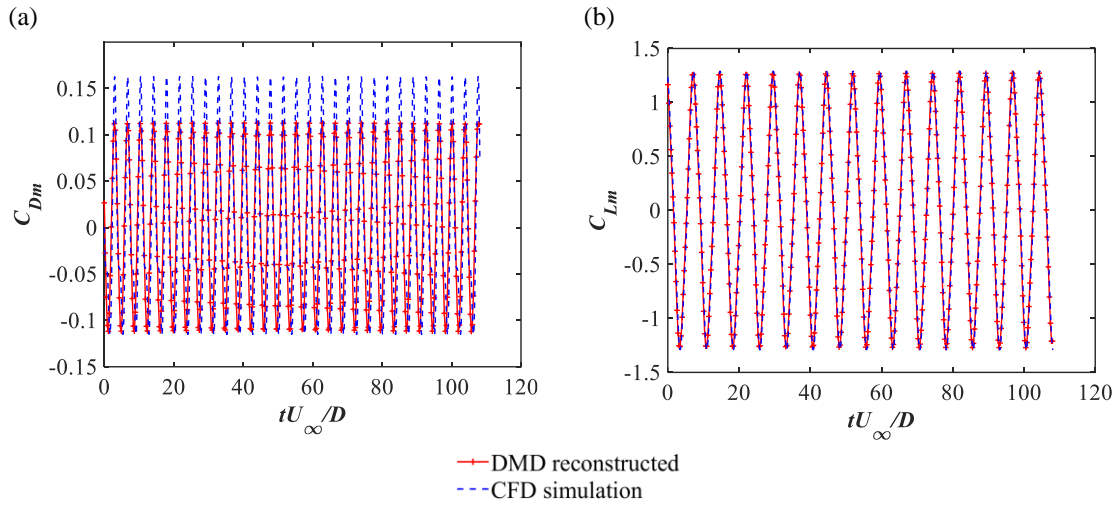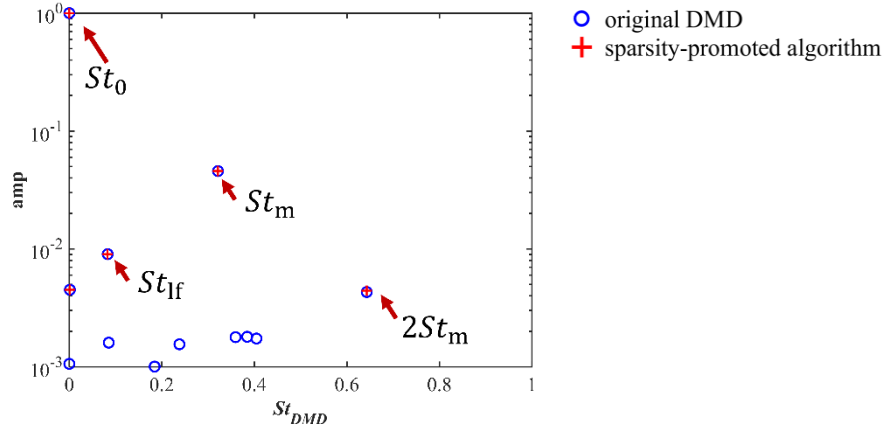

FIGURE 13: The time-histories of (a) the reconstructed body motion induced drag coefficient C_{Dm} (red crossings) compared with that obtained by carrying out the CFD simulation (blue dashed lines: the large cylinder); (b) the reconstructed volume integral of the lift coefficient C_{Lm} (red crossings) compared with that obtained by carrying out the CFD simulation (blue dashed lines) for Case 3.

12
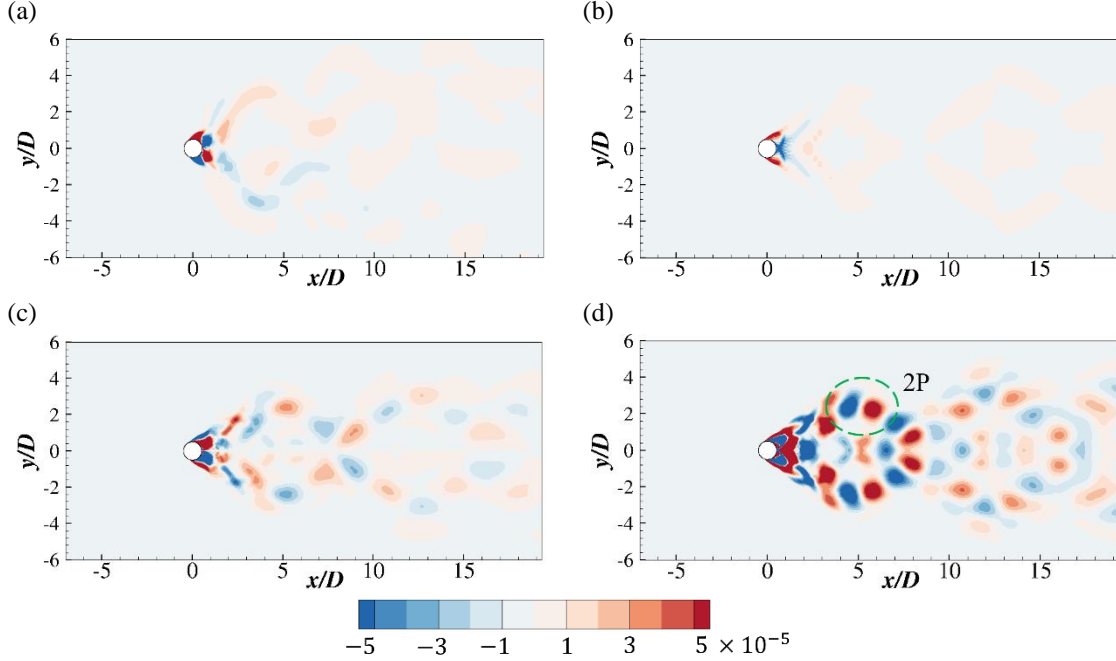
FIGURE 14: The spanwise vorticity contours of the extracted dominant DMD modes shown in Fig. 11 for Case 3: (a) the mean flow mode at St_0; (b) the mode at St_m; (c) the mode at $2St_m$; (d) the mode at $3St_m$.

For Case 4 with $U_r = 12$, a number of $N = 376$ snapshots equidistantly distributed with a time step of $\Delta t U_\infty / D = 0.08$ are also used. According to Serta et al. [3], at this U_r, the motion of the cylinder is desynchronized from the wake vortex shedding. The wake pattern can be classified as 2S. The DMD spectra for the $U_r = 12$ shown in Fig. 15 display a few dominant modes extracted by using the sparsity-promoting algorithm. The four extracted DMD modes are related to the mean flow, the vortex-shedding mode, its second harmonic and one low-frequency modulation mode at St_{lf}. The sum energy of the four dominant modes corresponds to almost 90% of the total energy. Due to the desynchronization of the cylinder motion from the vortex shedding, the cylinder vibration is weak. Therefore, there is no apparent wake flow mode directly induced by the motion vibration. The time-histories of the reconstructed $C_{D,\mathbf{u}\times\boldsymbol{\omega}}$, $C_{L,\mathbf{u}\times\boldsymbol{\omega}}$, C_{Dm} and C_{Lm} using the four dominant modes compared with those obtained by the CFD simulations are shown in Figs. 16 and 17. It can be seen that the reconstructed lift are almost the same as the simulations results due to the weak interaction between the flow and the cylinder vibration at this U_r. There is a small difference between the reconstructed drag force and the simulation results due to the truncation error. The spanwise vorticity of the modes for the four dominant modes are shown in Fig. 18. The traveling-wave behaviors in the wake flow for the vortex shedding mode and its second harmonic are similar to those behind a stationary cylinder as reported in Janocha et al. [22]. The low-frequency mode can represent the flapping motion of the shear layer, which is associated with the slow modulation of the wake flow.

13

FIGURE 15: The frequency spectra of the DMD modes for Case 4 and the dominant modes denoted by the arrows (blue circles: the modes obtained by using the original DMD method and red crossings: the modes obtained by applying the sparsity-promoted algorithm).
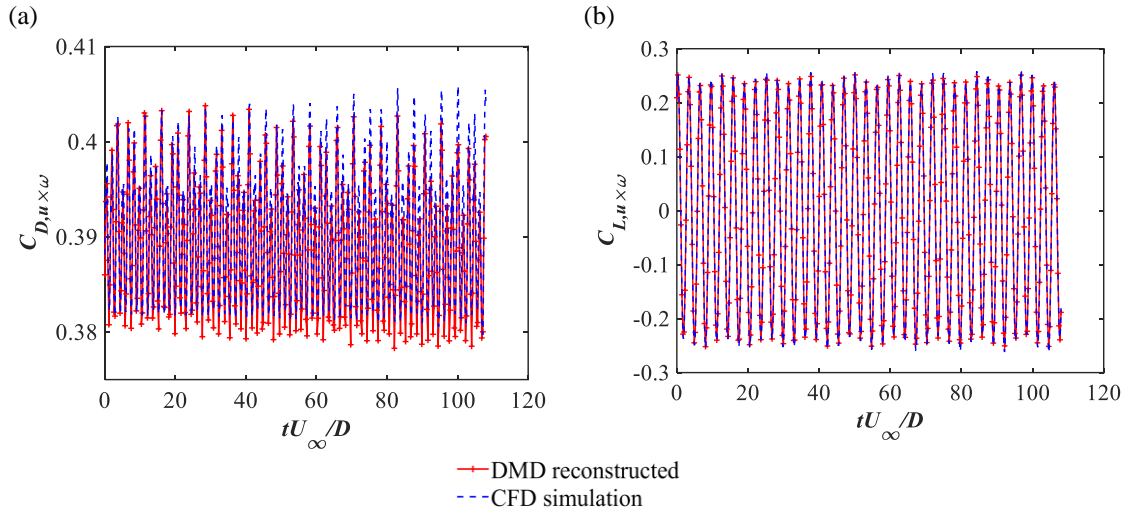
FIGURE 16: The time-histories of (a) the reconstructed volume integral of drag coefficient $C_{D,\mathbf{u}\times\boldsymbol{\omega}}$ (red crossings) compared with that obtained by carrying out the CFD simulation (blue dashed lines); (b) the reconstructed volume integral of the lift coefficient $C_{L,\mathbf{u}\times\boldsymbol{\omega}}$ (red crossings) compared with that obtained by carrying out the CFD simulation (blue dashed lines) for Case 4.
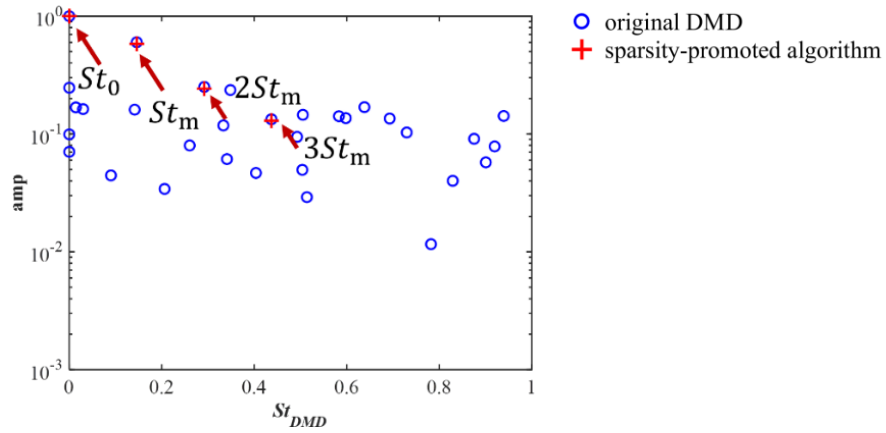
14
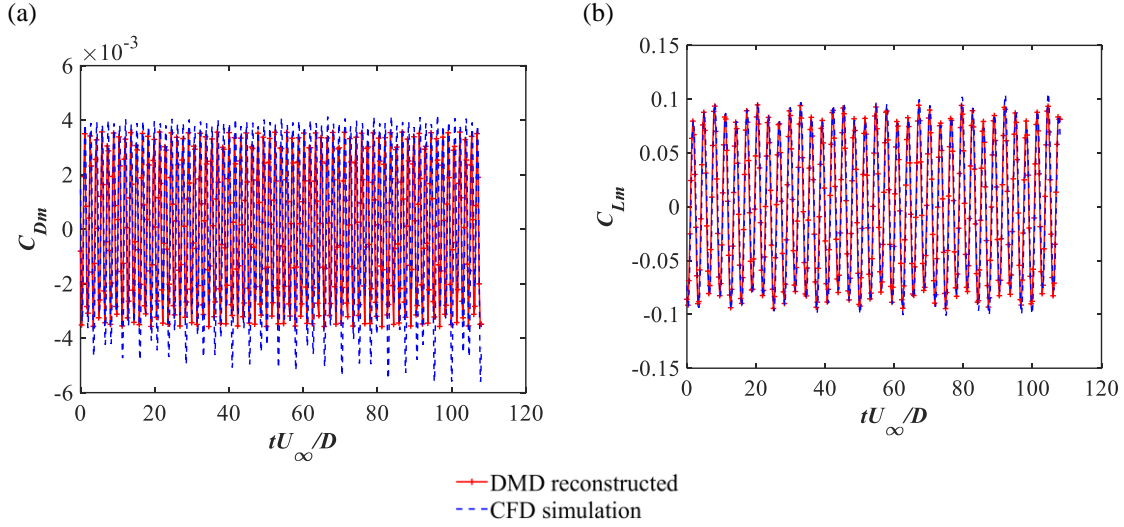
FIGURE 17: The time-histories of (a) the reconstructed body motion induced drag coefficient C_{Dm} (red crossings) compared with that obtained by carrying out the CFD simulation (blue dashed lines: the large cylinder); (b) the reconstructed volume integral of the lift coefficient C_{Lm} (red crossings) compared with that obtained by carrying out the CFD simulation (blue dashed lines) for Case 4.
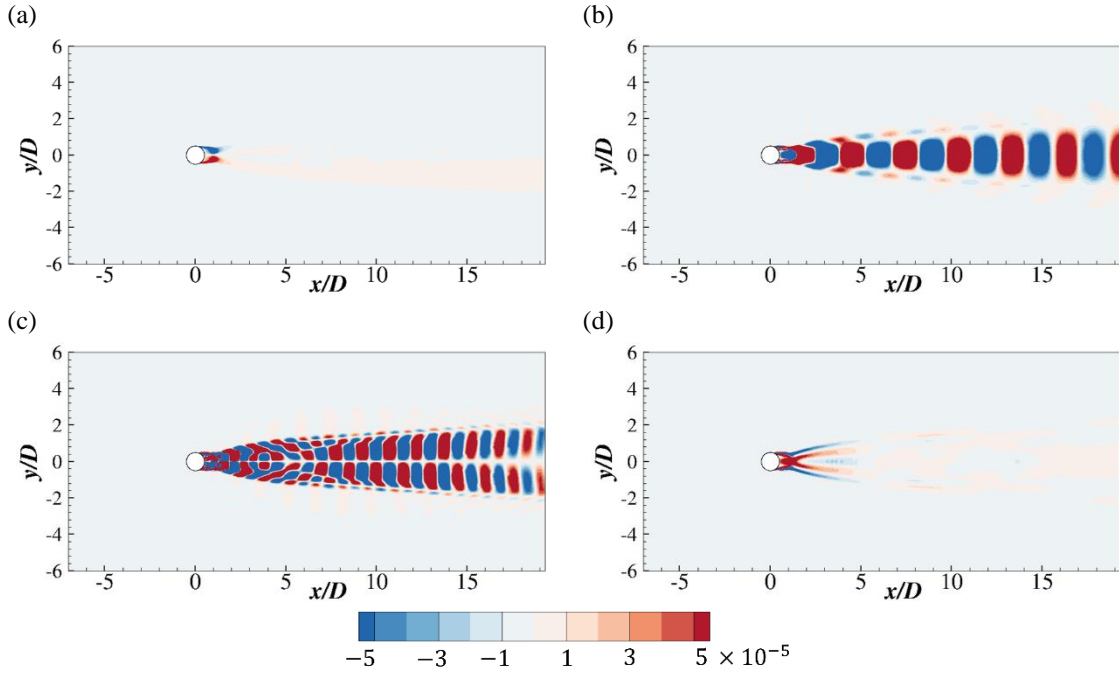

FIGURE 18: The spanwise vorticity contours of the extracted dominant DMD modes shown in Fig. 6 for Case 15: (a) the mean flow mode at St_0; (b) the mode at St_m; (c) the mode at $2St_m$; (d) the mode at St_{lf}.

For Case 5 with $U_r = 7$ for a piggyback pipeline, a number of $N = 524$ snapshots equidistantly distributed with a time step of $\Delta t U_\infty / D = 0.04$ are used. The DMD spectra for Case 5 are shown in Fig. 19. Similar to Cases 2 and 3, the four DMD modes related to the mean flow, the motion-induced flow, the vortex shedding frequency and their harmonics are extracted and they account for almost 80% of the total energy of the surrounding flow. The time-histories of the reconstructed $C_{D,\mathbf{u}\times\boldsymbol{\omega}}$, $C_{L,\mathbf{u}\times\boldsymbol{\omega}}$ and the motion

15

induced forces on the large cylinder C_{Dm1} and C_{Lm1} and those on the small one C_{Dm2} and C_{Lm2} using the four retained dominant modes are shown in Figs. 20 and 21 compared with those obtained carrying out the CFD simulation. It can be seen that the general temporal evolutions of these coefficients are well captured by using the four modes. The high-frequency oscillations in the time-histories of $C_{D,\mathbf{u}\times\boldsymbol{\omega}}$ and $C_{L,\mathbf{u}\times\boldsymbol{\omega}}$ of original simulations data are smoothed in the reconstructed results due to the truncation of modes with high frequencies. The spanwise vorticity of the modes for the four dominant modes are shown in Fig. 22. Due to the additional small cylinder, the symmetry of the wake flow in these modes disappears. Similar to Case 3, obvious vortex shedding pattern can be represented by the third harmonic mode. The upper part of the mode seems to display two rows of vortices and the lower part display pairs of vortices, which is related to a 2P flow pattern. For the motion induced mode, there is a strong small-scale surrounding flow around the piggyback due to the additional small cylinder.


FIGURE 19: The frequency spectra of the DMD modes for Case 5 and the dominant modes denoted by the arrows (blue circles: the modes obtained by using the original DMD method and red crossings: the modes obtained by applying the sparsity-promoted algorithm).
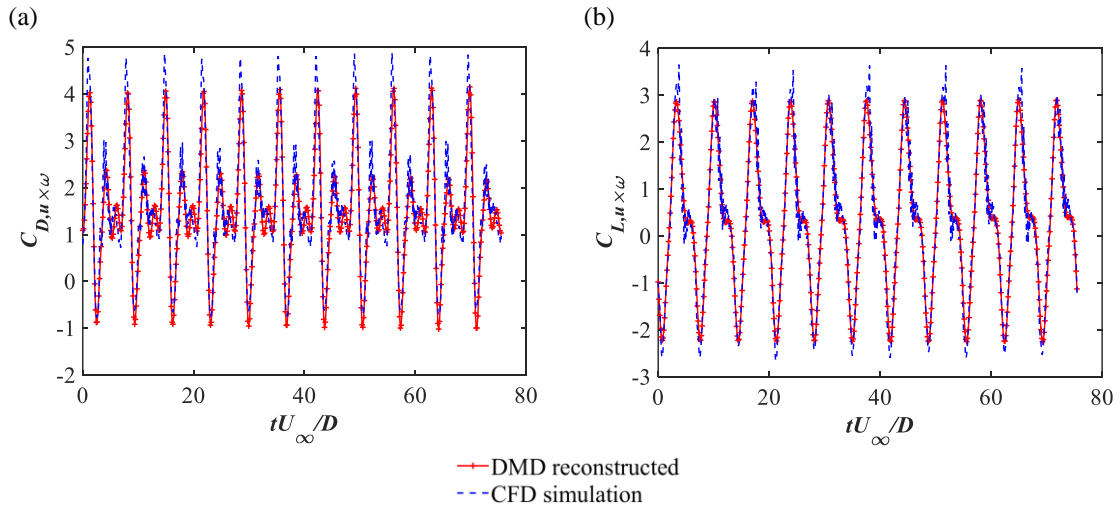

FIGURE 20: The time-histories of (a) the reconstructed volume integral of drag coefficient $C_{D,\mathbf{u}\times\boldsymbol{\omega}}$ (red crossings) compared with that obtained by carrying out the CFD simulation (blue dashed lines); (b) the reconstructed volume integral of the lift coefficient $C_{L,\mathbf{u}\times\boldsymbol{\omega}}$ (red crossings) compared with that obtained by carrying out the CFD simulation (blue dashed lines) for Case 5.
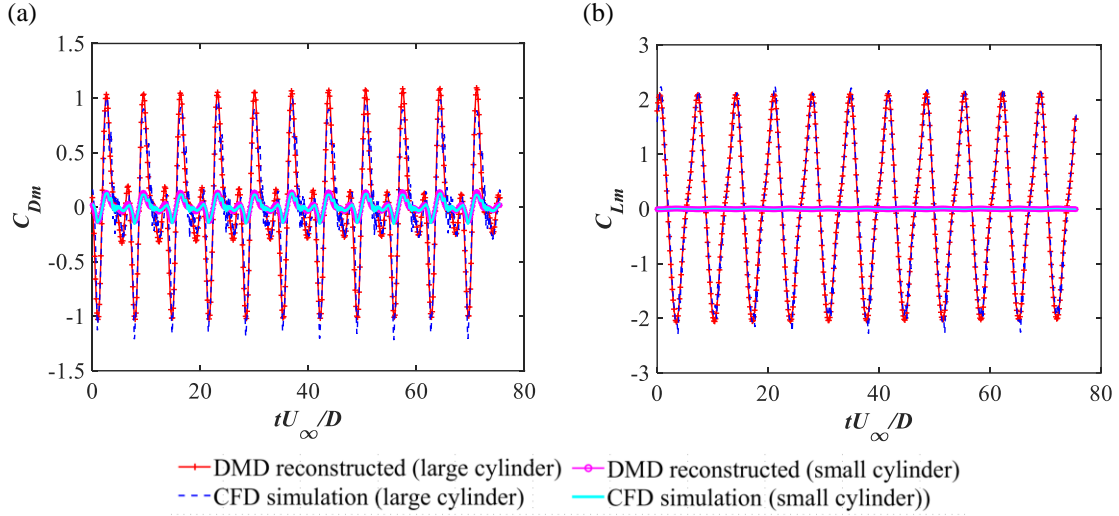
FIGURE 21: The time-histories of (a) the reconstructed body motion induced C_{Dm} (red crossings: the large cylinder C_{Dm1}; red circles: the small cylinder C_{Dm2}) compared with that obtained by carrying out the CFD simulation (blue dashed lines: the large cylinder; blue solid: the small cylinder); (b) the reconstructed body motion induced C_{Lm} (red crossings: the large cylinder C_{Lm1}; magenta circles: the small cylinder C_{Lm2}) compared with that obtained by carrying out the CFD simulation (blue dashed lines: the large cylinder; cyan solid: the small cylinder) for Case 5.
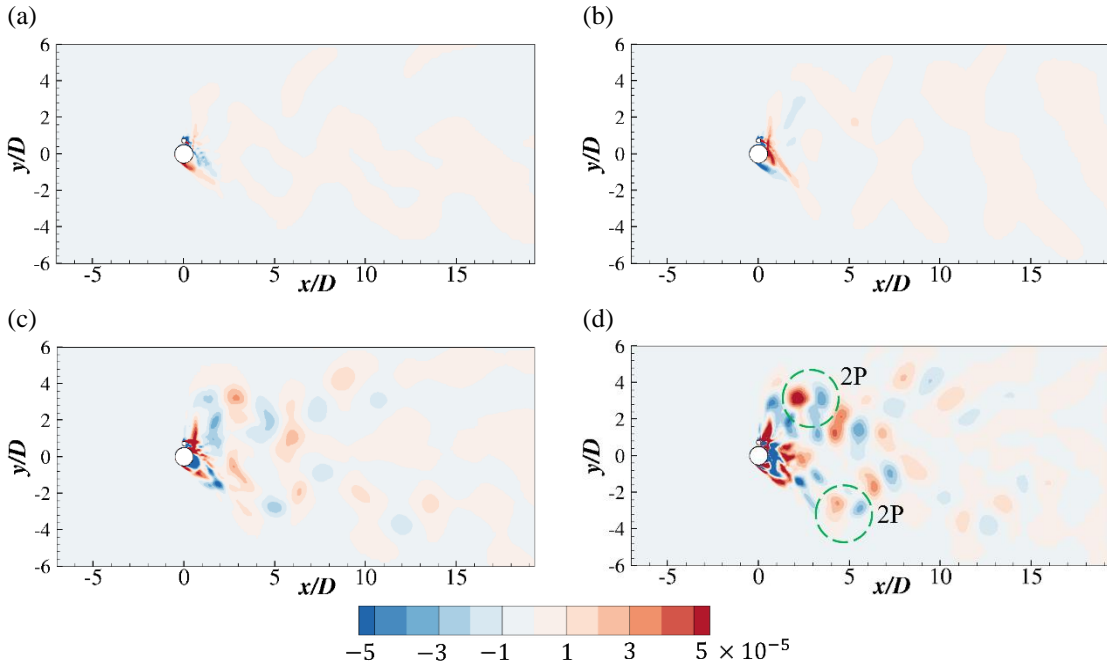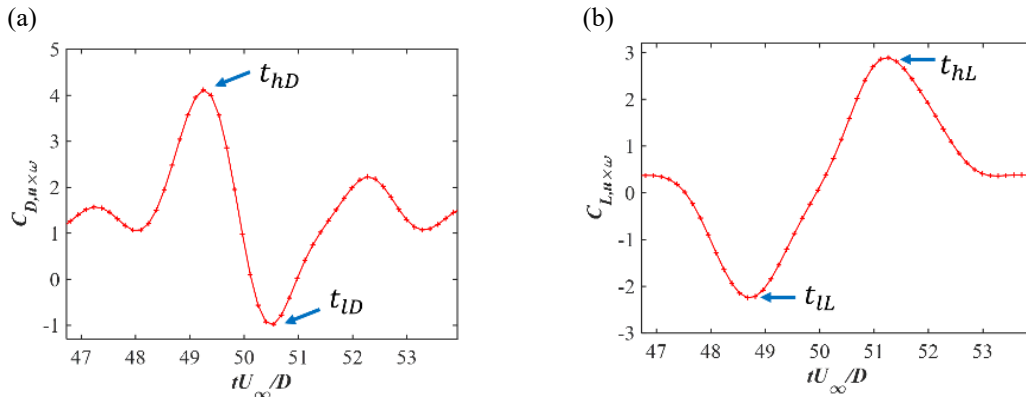

FIGURE 22: The spanwise vorticity contours of the extracted dominant DMD modes shown in Fig. 19 for Case 5: (a) the mean flow mode at St_0; (b) the mode at St_m; (c) the mode at $2St_m$; (d) the mode at $3St_m$.

The dominant DMD modes can be used to reconstruct the flow fields and quantify their contribution to the forces on the cylinders. The reconstructed flow fields of Case 5 by using the four dominant DMD are shown in Figs 24~28 at representative time steps. The selected time steps correspond to the highest and

lowest values of the reconstructed $C_{D,\mathbf{u}\times\boldsymbol{\omega}}$ and $C_{L,\mathbf{u}\times\boldsymbol{\omega}}$ as shown in Fig. 23. The contours of the reconstructed $(\mathbf{u}\times\boldsymbol{\omega})\cdot\nabla\phi_x$ and $(\mathbf{u}\times\boldsymbol{\omega})\cdot\nabla\phi_y$ are also shown at the corresponding time steps. It can be seen that the large-scale shedding 2P vortices pairs at $x/D \gtrsim 5$ are captured. Compared with the original flow fields obtained by numerical simulations, there are spurious small-scale flow structures on the side of the large cylinder where there should be no shedding vortices (for example as denoted in Fig 25 (a)). The emergence of these spurious and noisy flow structures is due to the reason that the DMD modes are extracted using snapshots spanning a number of vortex-shedding cycles and the temporally alternative appearance of the shedding vortices around both sides of the piggyback is revealed by these modes. Therefore, a larger number of modes are required in the reconstruction to remove the spurious flow structures. To evaluate the improvement of increasing the number of the modes for the reconstruction on the spurious noisy flow structures, the vorticity fields reconstructed by using 10 and 200 DMD modes at the same time step as in Figure 25 are shown in Figures 26 (a) and (b). It can be seen that when adding the number of DMD modes up to 10 and 200, the overall reconstructed flow fields are becoming progressively similar to the wake flow structures as the original CFD simulations shown in Figure 26 (c). Furthermore, the noisy flow structures around the shear layer in the lower side of the cylinder becomes much weaker compared with those reconstructed using only four dominant modes. The fringes of the wake vorticity also become smooth. Therefore, it suggests that adding more modes will improve the convergence of the reconstructed flow fields towards the CFD simulation results.

Furthermore, for the highest values of $C_{D,\mathbf{u}\times\boldsymbol{\omega}}$ as seen in Figure 24 (c), the main contribution to the total drag force is made by the distorted vortex street behind the small cylinder. Although there are spurious small-scale flow structures around the lower side of the large cylinder, they are of equal amplitudes with opposite signs. Therefore, the contribution made by these spurious flow structures is small. For the lowest values of $C_{D,\mathbf{u}\times\boldsymbol{\omega}}$ shown in Figure 25 (c), the straight vortex-shedding tilted towards the cross-flow direction behind the small cylinder make the main negative contribution to the total drag force. For the lowest value of $C_{L,\mathbf{u}\times\boldsymbol{\omega}}$ shown in Figure 27 (c), it can be observed that the main negative contribution comes from the distorted vortex street behind the small cylinder. It can be also seen that the reconstructed 2P vortex pair away from the cylinders also makes contribution to the total lift force. However, due to the counter rotation of the two vortices, there is not net contribution. For the highest $C_{L,\mathbf{u}\times\boldsymbol{\omega}}$ shown in Fig. 28 (c), although there are complicated structures around the near-wake region behind the two cylinders, there can be no large net contribution to the total lift force due to their opposite signs. Therefore, the main positive contribution may be due to shedding of the vortex pair from the previous cycle as denoted in Fig. 28 (c).

(a)   (b)

FIGURE 23: The selected time steps correspond to the highest and lowest values of the reconstructed (a) $C_{D,\mathbf{u}\times\boldsymbol{\omega}}$ at t_{hD} and t_{lD} and (b) $C_{L,\mathbf{u}\times\boldsymbol{\omega}}$ at t_{hL} and t_{lL}.
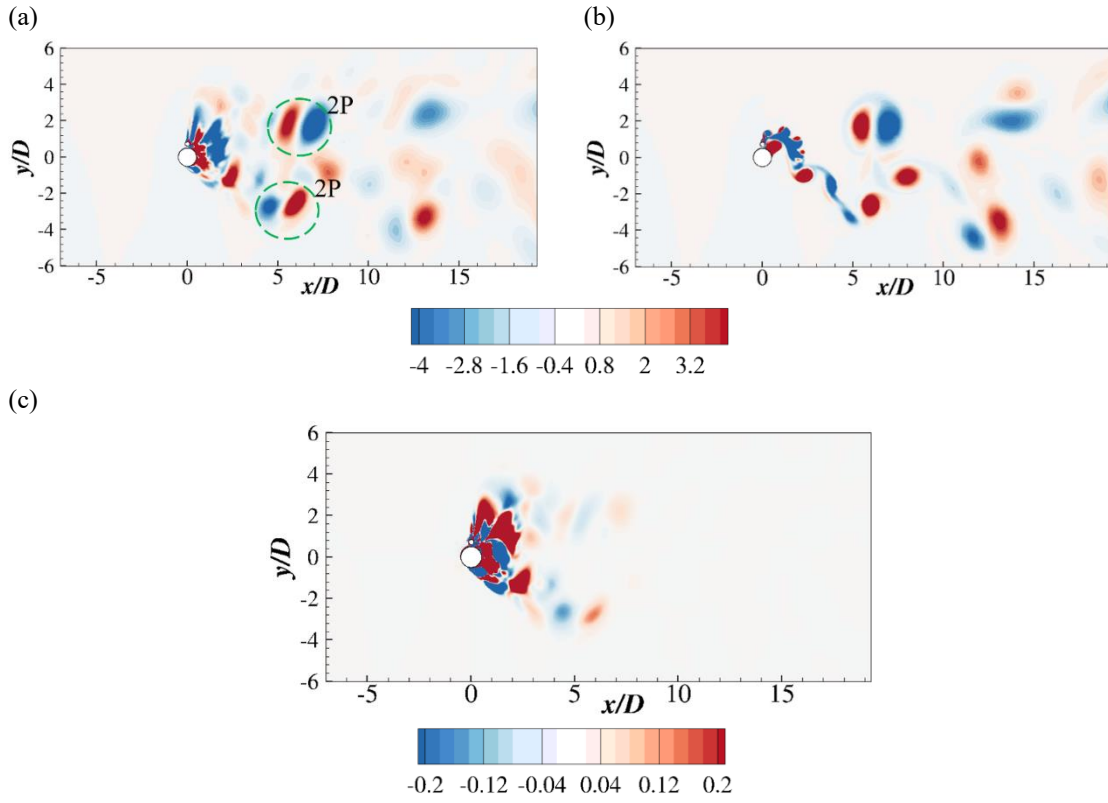
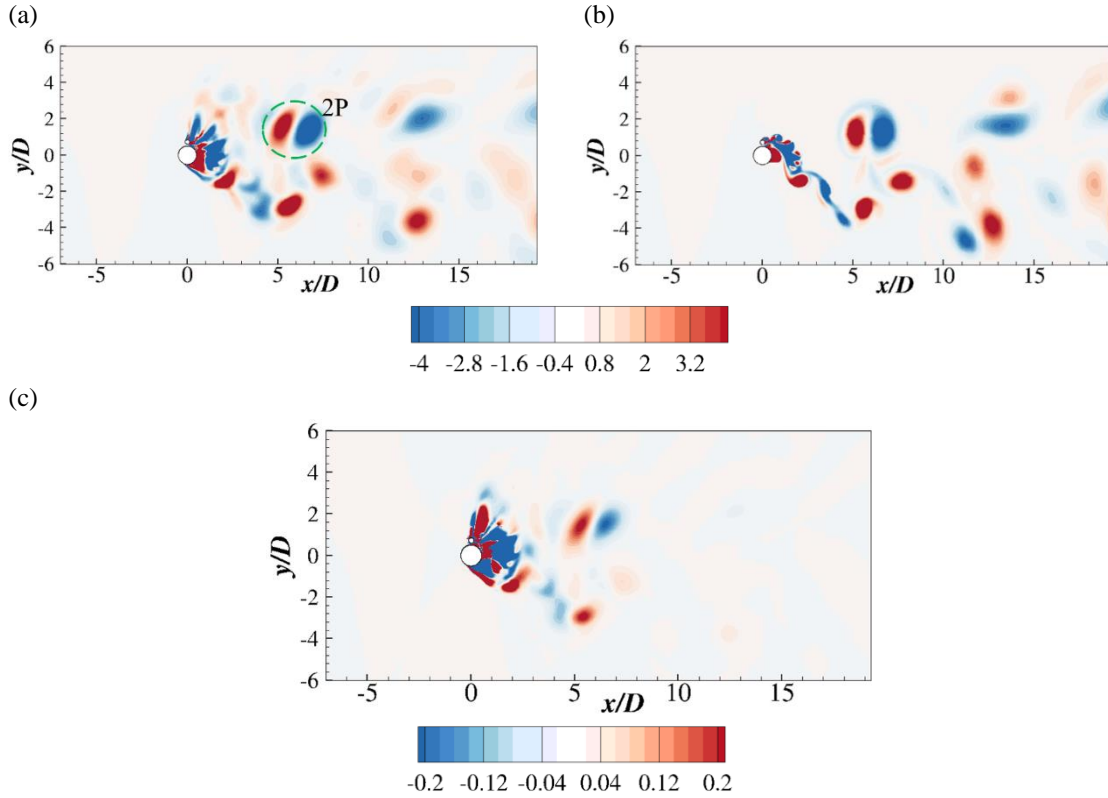**FIGURE 24:** The spanwise vorticity contours of (a) the reconstructed flow field; (b) the original flow field and (c) the contours of $(\mathbf{u} \times \boldsymbol{\omega}) \cdot \nabla \phi_x$ of the reconstructed flow field at t_{hD}.
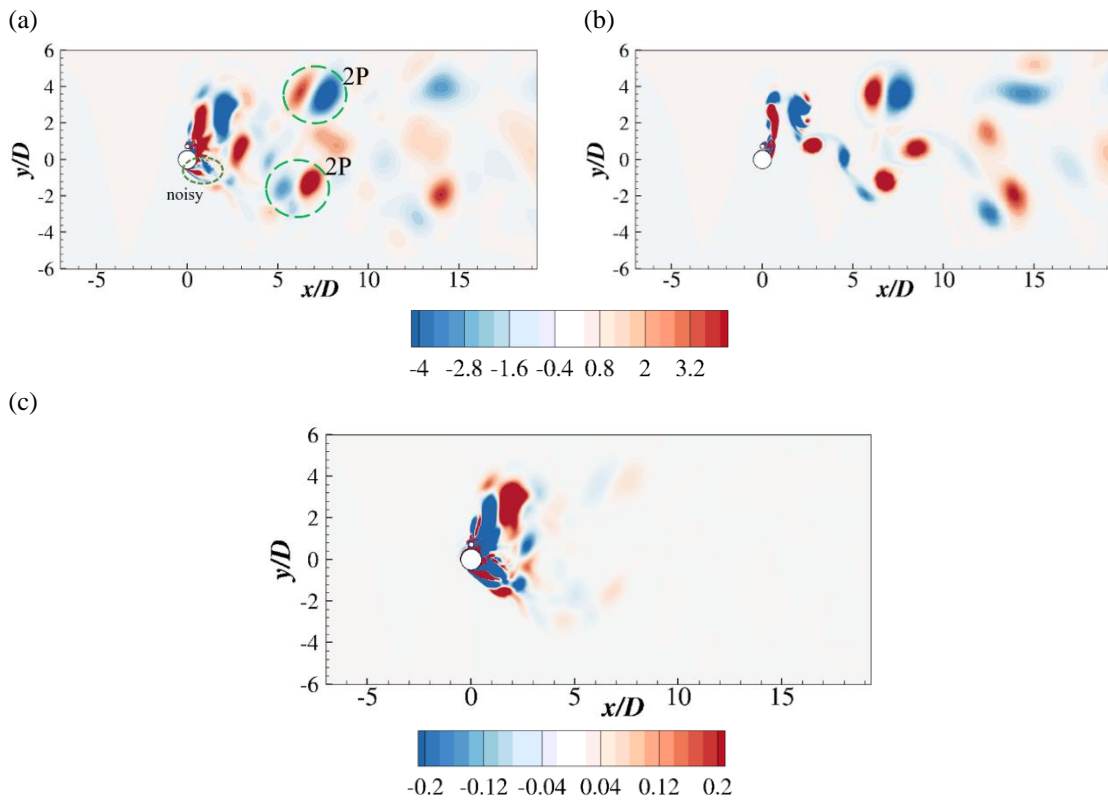
FIGURE 25: The spanwise vorticity contours of (a) the reconstructed flow field; (b) the original flow field and (c) the contours of $(\mathbf{u} \times \boldsymbol{\omega}) \cdot \nabla \phi_x$ of the reconstructed flow field at t_{lD}.
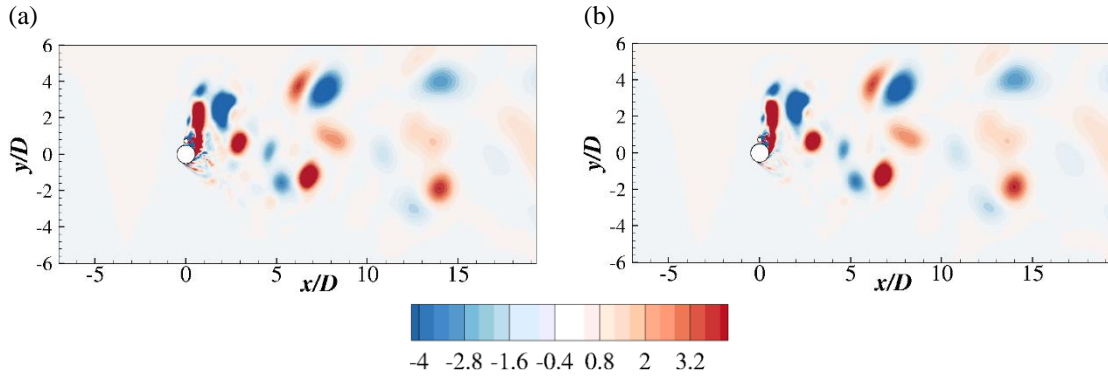
FIGURE 26: The spanwise vorticity contours of (a) the reconstructed flow field using 10 DMD modes; (b) the reconstructed flow field using 200 DMD modes at t_{lD}.
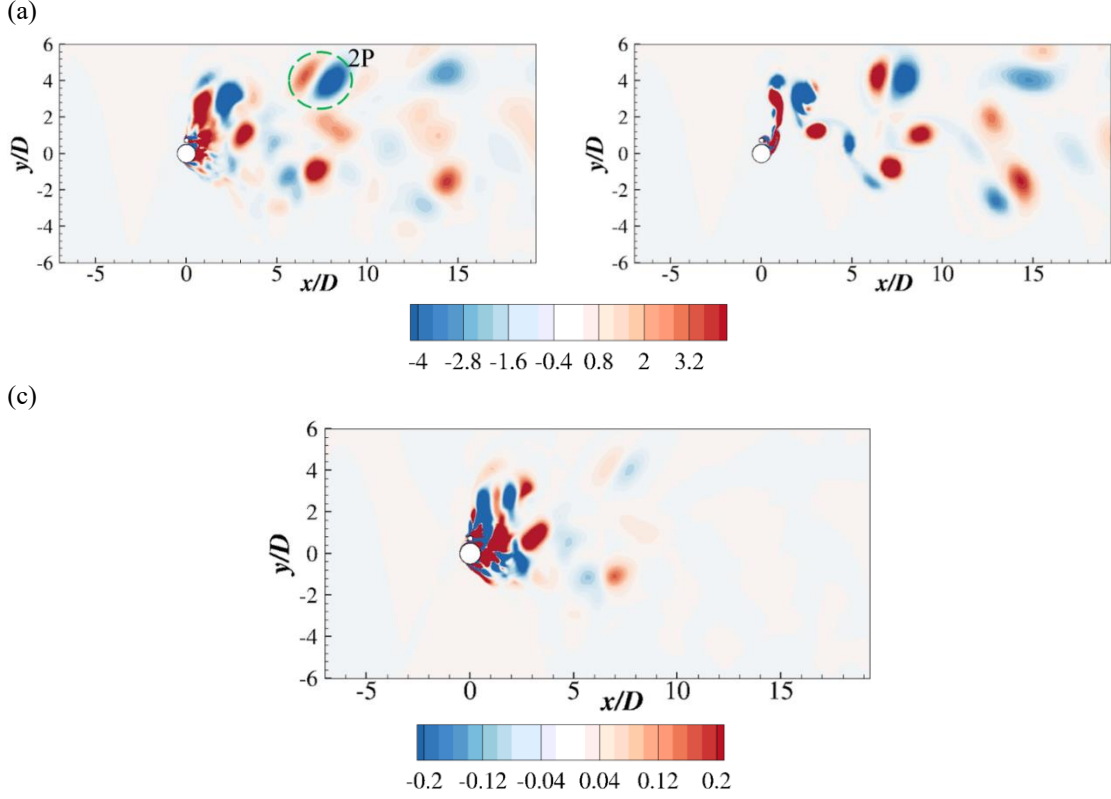

FIGURE 27: The spanwise vorticity contours of (a) the reconstructed flow field; (b) the original flow field and (c) the contours of $(\mathbf{u} \times \boldsymbol{\omega}) \cdot \nabla \phi_y$ of the reconstructed flow field at t_{lL}.

(a)

(c)

FIGURE 28: The spanwise vorticity contours of (a) the reconstructed flow field; (b) the original flow field and (c) the contours of $(\mathbf{u} \times \boldsymbol{\omega}) \cdot \nabla \phi_y$ of the reconstructed flow field at t_{hL}.

CONCLUSION

In the present study, the DMD analysis is performed on the wake flow behind cylinders undergoing VIV subjected to a uniform incoming flow. A moving reference frame method is employed in the present study to account for the moving boundary of vibrating cylinders. The dominant DMD modes associated with important flow features are identified using the sparsity-promoting algorithm. The hydrodynamic forces acting on the cylinders are estimated using these dominant modes through a force partitioning analysis. The main conclusion can be outlined as follows:

- For the analyzed cases, the vortex shedding mode as well as their harmonics are identified. Due to the vibration of the cylinders, two rows of alternative positive and negative vortices associated with the 2P vortex shedding pattern are observed. The large-scale wake flow behavior can be reconstructed using the dominant modes.

- For the low Re case, the contribution of each term to the total drag coefficient in the force partitioning analysis is well captured by the reconstructed flow field using the four dominant DMD modes. The drag coefficient $C_{D,\mathbf{u}\times\boldsymbol{\omega}}$ makes the dominant contribution to the total drag coefficient. The fluctuation amplitude is comparable to that of $C_{D,\mathbf{u}\times\boldsymbol{\omega}}$. The body motion induced lift force C_{Lm} makes the main contribution to the total lift coefficient.

- For the high Re case with $U_r = 6$, the general oscillation of the drag and lift coefficients can be reconstructed using the dominant modes. However, the chaotic behavior of their time histories cannot be represented using only a few dominant modes. For the single cylinder and the piggyback

configuration with $U_r = 7$, due to the regular wake flow and the motion pattern of the cylinders, the drag and lift coefficients can be well captured using the four dominant DMD modes.

References

[1]. Zhao, M., Cheng, L., An, H. and Lu, L., 2014. "Three-dimensional numerical simulation of vortex-induced vibration of an elastically mounted rigid circular cylinder in steady current," Journal of Fluids and Structures, 50, pp.292-311.

[2]. Janocha, M.J. and Ong, M.C., 2021. "Vortex-induced vibrations of piggyback pipelines near the horizontal plane wall in the upper transition regime," Marine Structures, 75, p.102872.

[3]. Serta, C.P.V., Janocha, M.J., Yin, G. and Ong, M.C., 2021. "Numerical simulations of flow-induced vibrations of two rigidly coupled cylinders with uneven diameters in the upper transition Reynolds number regime," Journal of Fluids and Structures, 105, p.103332.

[4]. Lumley, J.L., 1967. "The structure of inhomogeneous turbulent flows," Atmospheric turbulence and radio wave propagation, pp.166-178.

[5]. Schmid, P.J., 2010. "Dynamic mode decomposition of numerical and experimental data," Journal of fluid mechanics, 656, pp.5-28.

[6]. Liberge, E. and Hamdouni, A., 2010. "Reduced order modelling method via proper orthogonal decomposition (POD) for flow around an oscillating cylinder," Journal of fluids and structures, 26(2), pp.292-311.

[7]. Freno, B.A. and Cizmas, P.G., 2014. "A proper orthogonal decomposition method for nonlinear flows with deforming meshes," International Journal of Heat and Fluid Flow, 50, pp.145-159.

[8]. Yao, W. and Jaiman, R.K., 2017. "Model reduction and mechanism for the vortex-induced vibrations of bluff bodies," Journal of Fluid Mechanics, 827, pp.357-393.

[9]. Miyanawala, T.P. and Jaiman, R.K., 2019. "Decomposition of wake dynamics in fluid–structure interaction via low-dimensional models," Journal of Fluid Mechanics, 867, pp.723-764.

[10]. Wang, T.K. and Shoele, K., 2021. "Geometrically weighted modal decomposition techniques," Journal of Fluid Mechanics, 911.

[11]. Shinde, V., Longatte, E., Baj, F., Hoarau, Y. and Braza, M., 2016. "A Galerkin-free model reduction approach for the Navier–Stokes equations," Journal of Computational Physics, 309, pp.148-163.

[12]. Shinde, V., Longatte, E., Baj, F., Hoarau, Y. and Braza, M., 2019. "Galerkin-free model reduction for fluid-structure interaction using proper orthogonal decomposition," Journal of Computational Physics, 396, pp.579-595.

[13]. Shinde, V.J. and Gaitonde, D.V., 2021. "Lagrangian approach for modal analysis of fluid flows," Journal of Fluid Mechanics, 928.

[14]. Rowley, C.W., Mezić, I., Bagheri, S., Schlatter, P. and Henningson, D.S., 2009. "Spectral analysis of nonlinear flows," Journal of fluid mechanics, 641, pp.115-127.

[15]. Noack, B.R., Stankiewicz, W., Morzyński, M. and Schmid, P.J., 2016. "Recursive dynamic mode decomposition of transient and post-transient wake flows," Journal of Fluid Mechanics, 809, pp.843-872.

[16]. Towne, A., Schmidt, O.T. and Colonius, T., 2018. "Spectral proper orthogonal decomposition and its relationship to dynamic mode decomposition and resolvent analysis," Journal of Fluid Mechanics, 847, pp.821-867.

[17]. Ping, H., Zhu, H., Zhang, K., Zhou, D., Bao, Y., Xu, Y. and Han, Z., 2021. "Dynamic mode decomposition based analysis of flow past a transversely oscillating cylinder," Physics of Fluids, 33(3), p.033604.

[18]. Guzmán-Iñigo, J., Sodar, M.A. and Papadakis, G., 2019. "Data-based, reduced-order, dynamic estimator for reconstruction of nonlinear flows exhibiting limit-cycle oscillations," Physical Review Fluids, 4(11), p.114703.

[19]. Yu, M., Huang, W.X. and Xu, C.X., 2019. "Data-driven construction of a reduced-order model for supersonic boundary layer transition," Journal of Fluid Mechanics, 874, pp.1096-1114.

[20]. Menter, F.R., 1994. "Two-equation eddy-viscosity turbulence models for engineering applications," AIAA journal, 32(8), pp.1598-1605.

[21]. Yang, K., Cheng, L., An, H., Bassom, A.P. and Zhao, M., 2013. "The effect of a piggyback cylinder on the flow characteristics in oscillatory flow," Ocean engineering, 62, pp.45-55.

[22]. Janocha, M.J., Yin, G. and Ong, M.C., 2021. "Modal Analysis of Wake Behind Stationary and Vibrating Cylinders," Journal of Offshore Mechanics and Arctic Engineering, 143(4).

[23]. Jovanović, M.R., Schmid, P.J. and Nichols, J.W., 2014. "Sparsity-promoting dynamic mode decomposition," Physics of Fluids, 26(2), p.024103.

[24]. Statnikov, V., Sayadi, T., Meinke, M., Schmid, P. and Schröder, W., 2015. "Analysis of pressure perturbation sources on a generic space launcher after-body in supersonic flow using zonal turbulence modeling and dynamic mode decomposition," Physics of Fluids, 27(1), p.016103.

[25]. Wu, W., Meneveau, C. and Mittal, R., 2020. "Spatio-temporal dynamics of turbulent separation bubbles," Journal of Fluid Mechanics, 883.

[26]. Ohmichi, Y., 2017. "Preconditioned dynamic mode decomposition and mode selection algorithms for large datasets using incremental proper orthogonal decomposition," AIP Advances, 7(7), p.075318.

[27]. Matsumoto, D. and Indinger, T., 2017. "On-the-fly algorithm for dynamic mode decomposition using incremental singular value decomposition and total least squares," arXiv preprint arXiv:1703.11004.

[28]. Yin, G. and Ong, M.C., 2020. "On the wake flow behind a sphere in a pipe flow at low Reynolds numbers," Physics of Fluids, 32(10), p.103605.

[29]. Menon, K. and Mittal, R., 2020. "Dynamic mode decomposition based analysis of flow over a sinusoidally pitching airfoil," Journal of Fluids and Structures, 94, p.102886.

[30]. Chang, C.C., 1992. "Potential flow and forces for incompressible viscous flow," Proceedings of the Royal Society of London. Series A: Mathematical and Physical Sciences, 437(1901), pp.517-525.

[31]. Martín-Alcántara, A., Fernandez-Feria, R. and Sanmiguel-Rojas, E., 2015. "Vortex flow structures and interactions for the optimum thrust efficiency of a heaving airfoil at different mean angles of attack," Physics of Fluids, 27(7), p.073602.

[32]. Moriche, M., Flores, O. and García-Villalba, M., 2017. "On the aerodynamic forces on heaving and pitching airfoils at low Reynolds number," Journal of Fluid Mechanics, 828, pp.395-423.

[33]. Zhang, K., Hayostek, S., Amitay, M., He, W., Theofilis, V. and Taira, K., 2020. "On the formation of three-dimensional separated flows over wings under tip effects," Journal of Fluid Mechanics, 895.

[34]. Menon, K. and Mittal, R., 2021. "Quantitative analysis of the kinematics and induced aerodynamic loading of individual vortices in vortex-dominated flows: a computation and data-driven approach," Journal of Computational Physics, 443, p.110515.

[35]. Wang, S., He, G. and Liu, T., 2019. "Estimating lift from wake velocity data in flapping flight," Journal of Fluid Mechanics, 868, pp.501-537.

[36]. Tong, W., Yang, Y. and Wang, S., 2021. "Estimating thrust from shedding vortex surfaces in the wake of a flapping plate," Journal of Fluid Mechanics, 920.

[37]. Zheng, H., Xie, F., Zheng, Y., Ji, T. and Zhu, Z., 2019. "Propulsion performance of a two-dimensional flapping airfoil with wake map and dynamic mode decomposition analysis," Physical Review E, 99(6), p.063109.

[38]. Konstantinidis, E., Dorogi, D. and Baranyi, L., 2021. "Resonance in vortex-induced in-line vibration at low Reynolds numbers," Journal of Fluid Mechanics, 907.